



Article

Permanent Magnet Assisted Synchronous Reluctance Motor for Subway Trains

Vladimir Dmitrievskii ¹, Vadim Kazakbaev ¹, Vladimir Prakht ^{1,*} and Alecksey Anuchin ²

¹ Department of Electrical Engineering, Ural Federal University, 620002 Yekaterinburg, Russia; vladimir.dmitrievsky@urfu.ru (V.D.); vadim.kazakbaev@urfu.ru (V.K.)

² Department of Electric Drives, Moscow Power Engineering Institute, 111250 Moscow, Russia; anuchinas@mpei.ru

* Correspondence: va.prakht@urfu.ru

Abstract: With the growing demand and projected shortage of rare earth elements in the near future, the urgent task of developing energy-efficient electrical equipment with less dependence on rare earth magnets has become paramount. The use of permanent magnet-assisted synchronous reluctance motors (PMSynRMs), which reduce the consumption of rare earth magnets, can help solve this problem. This article presents a theoretical analysis of the characteristics of PMSynRM in a subway train drive. Options with rare earth and ferrite magnets are considered. Optimization of the motor designs considering the train movement cycle is carried out using the Nelder-Mead method. Characteristics of the motors, such as losses, torque ripple, and inverter power rating, as well as the mass and cost of active materials, are compared.

Keywords: AC machines; brushless motors; electric vehicles; electromagnetic modeling; permanent magnet motors; public transportation; reluctance motors; traction motor



Citation: Dmitrievskii, V.; Kazakbaev, V.; Prakht, V.; Anuchin, A. Permanent Magnet Assisted Synchronous Reluctance Motor for Subway Trains. *World Electr. Veh. J.* **2024**, *15*, 417. <https://doi.org/10.3390/wevj15090417>

Academic Editors: Xinmin Li and Liyan Guo

Received: 16 August 2024

Revised: 7 September 2024

Accepted: 10 September 2024

Published: 13 September 2024



Copyright: © 2024 by the authors. Published by MDPI on behalf of the World Electric Vehicle Association. Licensee MDPI, Basel, Switzerland. This article is an open access article distributed under the terms and conditions of the Creative Commons Attribution (CC BY) license (<https://creativecommons.org/licenses/by/4.0/>).

1. Introduction

Subway traction drives typically use traditional induction motors. However, some industry leaders have begun using synchronous motors in new subway trains. For example, permanent magnet synchronous motors from Alstom [1] and Siemens [2], Toshiba [3], or the synchronous reluctance motor from Mitsubishi Electric [4].

Note that permanent magnet synchronous motors (PMSMs) have a smaller mass compared to induction motors, which is very important for traction drives. In addition, PMSMs have a smaller rotor weight than that of induction motors. This is especially important in subway drives, as it allows to increase the service life of bearings and increase the interval between maintenance of the bearing unit. Additionally, the use of PMSMs instead of induction motors allows to significantly reduce electrical losses and heating.

Permanent magnet-assisted synchronous reluctance motors (PMSynRMs) are comparable in performance to internal magnet synchronous motors (IPMs) [5,6], requiring substantially fewer rare earth permanent magnets [7,8], or using inexpensive ferrite magnets instead of rare-earth ones [9,10]. Since the shortage of rare-earth permanent magnets is predicted to increase in the near future [11,12], replacing IPMs with PMSynRMs in a number of applications, such as electric vehicles [6], is becoming promising. There are quite a lot of examples in the literature comparing different PMSynRM configurations for various applications.

Thus, in [13], a comparison of the characteristics of a synchronous reluctance motor (SynRM) without permanent magnets and a ferrite-assisted SynRM (FaSynRM) is presented. The effect of using a hybrid star-delta winding for both designs is also discussed. It is shown that among the motors under consideration, the FaSynRM with star-delta winding has the highest torque capacity and the widest constant power speed range (CPSR) of approximately 3.

Article [14] presents a comparison between a rare-earth assisted SynRM (REaSynRM) and a hybrid RE/FaSynRM in a passenger vehicle drive with a CPSR of 3. It is shown that the FaSynRM has better energy efficiency, greater rotor strength, and provides a higher output power at speeds above nominal.

Article [15] presents a theoretical comparison of the performance of an IPM and a PMASynRM in a passenger car drive with CPSR of 3.5:1. The study concludes that the PMASynRM is very close in performance to the IPM, while significantly reducing active material costs and demonstrating reduced maximum rotor operating temperature.

However, the prospects for using PMASynRMs in subway train drives have not yet been widely discussed in the literature. There are known projects using SynRMs without permanent magnets in a subway train drive [4]. Meanwhile, PMASynRMs can also be promising in this application since they also reduce/eliminate the need for RE while being more compact and requiring an inverter of a lower rating.

This article presents a study of the characteristics of PMASynRM in a subway train drive. In this case, both REaSynRM and FaSynRM designs are considered. The optimal design results for the REaSynRM are presented in this paper. The characteristics of the FaSynRM are adapted from the authors' previous study [16]. The characteristics of the considered motors are compared, such as power losses, torque ripple, and inverter power, as well as the mass and cost of active materials. The motor optimization criteria are losses in the operating cycle of a metro train, maximum motor current, torque ripple, rotor mass, and permanent magnet mass. The mass of the rotor is considered since it affects the service life of the bearings. Since rare-earth permanent magnets are the most expensive material, the mass of rare-earth permanent magnets is included in the optimization criteria to reduce the cost of active materials.

The contribution of this paper is the theoretical comparison of REaSynRM and FaSynRM in subway drives, considering the preliminary optimization of their losses in the subway train motion cycle. For this purpose, the REaSynRM parameterization presented in the article was proposed.

The use of the population-free Nelder–Mead method can significantly reduce computational costs when considering a relatively large number of operating points of the motion cycle during the optimization process.

As a result of optimization, such a reduction in the mass of rare-earth magnets in the REaSynRM is achieved that their price is approximately equal to the price of ferrite magnets in the FaSynRM.

2. Considering the Train Movement Cycle in the Motor Optimization

When designing and optimizing a traction motor, it is important to consider the characteristics and operating conditions of the vehicle for which this motor is intended. In the simplest case, designers consider the characteristics of the motor at maximum torque and maximum speed. To increase energy savings, it is important to consider the time diagram of load parameters during the driving cycle [17,18]. However, load conditions (operating mode, shaft torque, and rotational speed) usually vary greatly during the operating cycle, making the selection of a single equivalent point representing multiple operating points not entirely relevant. One solution to this problem is to consider during optimization the points of the driving cycle that join different stages of movement [19,20] and carry out optimization at these points. The trapezoidal quadrature formula can be used to estimate the average values [21].

Table 1 shows six equivalent points at which the subway train motor is optimized. These six equivalent operating points are derived from the following. When moving from station to station, the train goes through stages, shown in Figure 1 and in Table 1. The blue numbers in this figure correspond to the various operating points shown in Table 1:

- (1) Acceleration while maintaining a constant torque $T_0 = 1240 \text{ N}\cdot\text{m}$ to a speed $n_m = 1427 \text{ rpm}$ (plot sections 4–5);
- (2) Acceleration with constant power up to speed $n_{max} = 4280 \text{ rpm}$ (sections 5–1);

- (3) Movement by inertia at approximately constant speed (sections 1–2); the model does not take into account friction, and the speed at this stage is assumed to be exactly constant.
- (4) Braking from speed n_{max} to speed $n_g = 2854$ rpm with a constant power (sections 2–3);
- (5) Braking with torque $T_0 = 1240$ N·m to the stop (sections 3–4).

Table 1. Operating cycle of the subway train drive.

Stage	Stage Name	Duration, s
4–5	Acceleration with a constant torque	6.9
5–1	Acceleration with a constant power	27.8
0	Coasting at a steady speed	57.3
2–3	Deceleration with a constant power	8.7
3–4	Deceleration with a constant torque	13.9

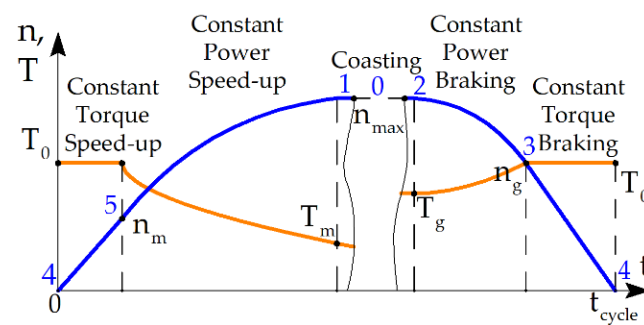


Figure 1. Graphical representation of the rotational speed (blue line) and torque (orange line) generated by the traction motor of a subway train as it moves from station to station. Based on the diagram from Ref. [22].

To calculate the weight coefficients w_i of the equivalent points, the diagram presented in Figure 2 is used. In this figure, the numbers of the various operating points from Table 2 are indicated in blue font. It shows the points of the braking (generator) mode to the left of the ordinate axis. To the right of the ordinate are the points of the motor mode. Point 0 on the ordinate axis is necessary to consider losses in the motor when moving by inertia (losses in steel from the flux of permanent magnets and mechanical losses), which is important because of the longest duration of this stage. If coasting takes up 50% of the time required to travel between stations, integrating the speed shows that coasting takes up 63.3% of the total distance.

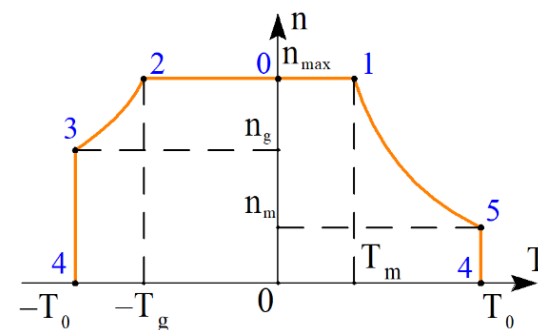


Figure 2. Requirements for the torque-speed characteristic of the traction motor for the subway train, on which the numbers of the various operating points from Table 1 are indicated in blue font. Based on the diagram from Ref. [22].

Table 2. Points highlighted from the operating cycle which are examined to ensure optimal performance and efficiency.

Operating Point, i	Operating Point Name	Speed, rpm	Torque, N·m	w_i	k_i	w^{ex}_i *
0	Coasting mode; maximum speed	4280	0	-	-	0.5
1	Driving mode; maximum speed	4280	413.4	0.363	0.97	0.181
2	Braking mode; maximum speed	4280	826.9	0.091	0.99	0.046
3	Braking mode; changing from constant power to constant torque	2854	1240	0.182	1.1	0.091
4	Zero speed	0	1240	0.182	0.97	0.091
5	Driving mode; changing from maximum torque to constant power	1427	1240	0.182	0.97	0.091

Note: * w^{ex}_i represents the weight coefficient for the i -th operating point, which indicates the proportion of time that the i -th operating point occupies within the overall movement cycle.

These weighting factors are specifically defined as follows:

$$w^{ex}_0 = 1/2; w^{ex}_i = w_i/2, i = 1, 2, 3, 4, 5. \quad (1)$$

The calculation of weights w_i is described in more detail in [21]. The average loss over the driving cycle, denoted as $\langle P_{loss} \rangle$, is calculated using the formula:

$$\langle P_{loss} \rangle = \sum (w^{ex}_i \cdot P_{loss\ i}), \quad (2)$$

where $P_{loss\ i}$ represents the total loss at the i -th operating point.

The maximum available voltages V_i are given by the factors $k_i = V_i / V_{DC\ rated}$, where $V_{DC\ rated}$ is the nominal DC voltage of 750 V, are not the same at different operating points. When operating in generator or motor mode, the output voltage levels can be affected by various factors, such as voltage drop across the power switching device. To take this into account, different values of coefficient k_i are used. The parameters k_2 , k_4 , and k_5 are set to 0.97 to account for the voltage drop across the switches in these cases. k_1 is set to 0.99, which reflects the increase in DC voltage in generator mode. At operating point 2 (generator mode), k_2 can be selected more than in motor modes 1, 4, and 5 due to battery charge recovery.

3. Main Design Features of the Motor and Traction Inverter

Figure 3 sketches of the REaSynRM and FaSynRM designs. Table 3 shows the main characteristics of the motor designs under consideration. It can be noted that in the case of the REaSynRM, the dimensions of the magnets are much smaller. While the thickness of the rotor flux barriers is not significantly less, they are narrowed in the magnet mounting segments.

Rare earth magnets have high residual flux density and coercivity. High coercivity allows the thickness of the magnets to be reduced without the risk of irreversible demagnetization. Due to their high residual flux density, rare earth magnets produce sufficient magnetic flux even when placed into a short section of magnetic barriers. Therefore, this study considers an REaSynRM rotor design in which fairly wide magnetic barriers have small narrowings to accommodate magnets. Sufficiently wide barriers make it possible to increase the magnetic anisotropy of the REaSynRM, and since the narrowing area is small, the magnetic anisotropy suffers only slightly.

The motor winding pattern is also visually represented in Figure 3 with letters from A to C to denote their sequential order. The inclusion of a minus sign in Figure 3 indicates a reversal in the current direction within a winding layer. Both designs of PMSynRM under consideration have 8 poles, 48 slots, and 3 phases. The number of slots per pole and phase is equal to $q = 48 / (8 \times 3) = 2$.

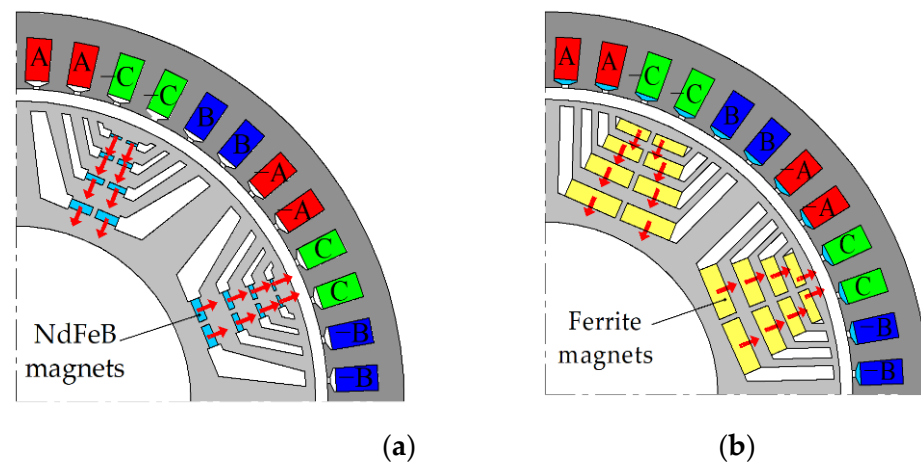


Figure 3. Motor design representation, 2-pole area, magnetization of the permanent magnets is marked with red arrows: (a) rare-earth-assisted synchronous reluctance motor (REaSynRM); (b) ferrite-assisted synchronous reluctance motor (FaSynRM).

Table 3. Design features of the PMASynRMs.

Parameter	REaSynRM	FaSynRM [16]
Phase number		3
Pole number		8
Magnet grade	N40H	Y30H-2
Steel grade		M270-35A
Steel thickness, mm		0.35
Stator slot number		48
Number of the armature winding layers		1
Number of the stator slots per pole and phase q		2
Rotor flux barrier number per pole		4

PMASynRMs with different numbers of flux barriers can have high performance [23]. For the PMASynRM in this study, a rather large number of 4 was chosen, since it is known that further increasing the number of barriers does not lead to a significant increase in the performance of SynRM and PMASynRM but reduces their mechanical strength and complicates their manufacturing [23].

The number of poles was chosen to be 8 for fair comparison with the results of other types of subway motors obtained in our previous studies [16,21].

Figure 4 depicts the power supply circuit for the traction motor, consisting of a conventional three-phase inverter designed for driving the armature winding of the PMASynRM.

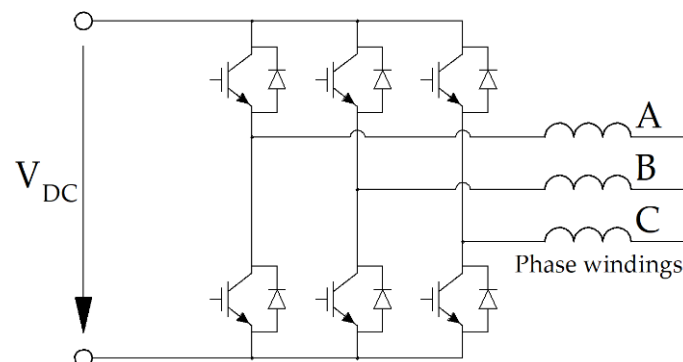


Figure 4. Subway train traction motor inverter. Armature phase windings are indicated with A, B, and C.

4. Objective Function and Optimization Procedure

In the process of optimizing the REaSynRM, the objective functions are minimized using the Nelder–Mead method. Although the Nelder–Mead method is a local optimization technique, it is particularly effective when initiated with well-chosen design parameters. A key benefit of this method over population-based algorithms, such as genetic algorithms and particle swarm optimization [24,25], lies in their significantly shorter computational time. This efficiency is especially important when optimizing many parameters or applying more complex optimization criteria, which is critical for improving the performance of electric machines across various operational conditions.

The motor's external diameter is constrained by the dimensions of the car bogie, requiring compatibility with existing commercial induction motors. The optimization process primarily aims to minimize losses within the duty cycle, as illustrated in Figure 1, while also reducing the current rating for the power modules in the traction inverter. This dual focus not only enhances the overall efficiency of the machine but also contributes to cost reduction.

The objective functions of both machines are similar, although that of the FaSyRM has an additional penalty term in the case of demagnetization of the magnets. At the same time, due to the high coercivity of rare earth magnets, their demagnetization is not checked during the REaSynRM optimization. This check was carried out only for the REaSynRM final design.

The optimization goals for a subway train's traction motor can be broken down into the following:

- (1) Firstly, there is a focus on minimizing the overall energy loss during operation, represented by the average loss factor $\langle P_{loss} \rangle$. This value is derived from an assessment of losses across various operating points, with weights assigned according to their relative importance;
- (2) Secondly, the algorithm is aimed at reducing the peak current I_{arm} consumed by the motor armature winding at operating points 1–5, since minimizing this value allows for reducing the cost of power switches of the traction inverter at a given voltage limit. The power factor was not considered as an objective because it may take high values at high current values when the available voltage is not used enough;
- (3) It is also important to reduce the motor torque ripple TR_i at operating points 1–5 to ensure a longer lifetime of the powertrain;
- (4) Minimizing the mass of the rotor M_{rot} (its magnetic core plus magnets). The rotor mass is added to the optimization function, since it affects the service life of the bearings, and an excessively large rotor mass will lead to unreasonably rapid failure of the bearings;
- (5) Minimizing the mass of the permanent magnets M_{mag} . The mass of permanent magnets is added to the optimization function, since permanent magnets are the most expensive material in the magnetic core, and their excessive use will lead to an unjustified increase in the cost of the machine.

The Nelder–Mead method, also known as the downhill simplex algorithm, is an unconstrained optimization technique, meaning it does not directly enforce constraints on variable parameters. However, as designs approach infeasibility, the objective function naturally increases, discouraging unfeasible solutions.

The objective function representing the above-described goals has the following form:

$$F = \ln(\langle P_{loss} \rangle) + 0.7\ln(\max(I_{arm\ i})) + 0.1\ln(\max(TR_i)) + 0.2\ln(M_{rot}) + 0.2\ln(M_{mag}). \quad (3)$$

The weight coefficients used in Equations (3) and (4) (specifically, 1, 0.7, 0.1, 0.2, and 0.2) are applied to represent the relative importance of various optimization objectives. These values reflect the priorities assigned to each objective based on the authors' extensive experience in designing similar machines. For instance, the coefficient of 0.7 indicates

that a 1% reduction in maximum current is considered equivalent to a 0.7% decrease in average loss, illustrating the balance between different performance metrics within the optimization process.

Relatively less importance is attributed to the goal of minimizing torque ripple. Similarly, the constants 0.2 and 0.2 reflect the values of the goals minimizing the rotor and magnet masses.

These values reflect the approximate relative priorities assigned to each optimization goal, based on the author's extensive experience in designing similar machines.

The optimization process for the REaSynRM involves minimizing losses even during coasting mode, where the motor is turned off, as illustrated in Figure 1. Despite the motor being turned off, losses generated by permanent magnets within the magnetic core do not disappear completely. This is particularly significant because the motor spends a considerable amount of time in this phase during the operational cycle.

The number of turns in the armature winding, denoted as N_{sec} , is selected so that $V_{DC\ rated} = \max(V_i/k_i)$ [26]. A crucial aspect of electric motor development is the recognition of the discrete nature of certain parameters, such as the number of turns N_{sec} in the armature winding coil and the standardized dimensions of the rectangular wire's width and height, as specified in [21]. However, this study diverges from treating these values strictly as discrete, allowing them to take positive real values. This approach provides a more unbiased evaluation. While technological limitations may necessitate adjustments from the calculated optimal parameters (e.g., the number of turns in a coil must be an integer), the goal in practical electric machine implementation is to ensure that the actual parameters are as close as possible to the theoretical optimum.

The optimization process employs the Nelder–Mead method [27], using the `fminsearch` procedure, which is carried out within the MATLAB R2020b software environment, as detailed in [28]. The primary aim of the `fminsearch(F, x0)` procedure is to iteratively adjust the vector x , which represents the parameters of the electric machine, in order to minimize the objective function F . The vector x_0 provides the initial values for these parameters, guiding the optimization process toward an optimal solution.

The calculations are performed based on a series of magnetostatic finite element model (FEM) problems. The losses are calculated in postprocessing. In FEM modeling, the properties of electric steel are taken into account conventionally by specifying the magnetization curve $B(H)$ corresponding to the steel grade under consideration.

When calculating losses in the stator and rotor cores, it is taken into account that the magnetic flux is not sinusoidal, and a conventional method is used based on the magnitude of the flux density vector at various rotor positions calculated using FEM [29]. The calculation time for one machine candidate (including five operating points) on a laptop with a Core i5 4210U processor is 20 min.

5. REaSynRM Optimization Results

5.1. REaSynRM Optimization Parameters

Figure 5 shows a detailed visualization of the REaSynRM geometry, highlighting various critical parameters. The rotor of the REaSynRM features four distinct magnetic flux barriers per pole, which are numbered sequentially from 1 to 4, starting from the outermost barrier and progressing to the innermost one. This specific arrangement is depicted in Figure 5b. To maintain the rotor's structural integrity, internal ribs are strategically placed at the midpoint of each flux barrier, with their thicknesses denoted as $h_{in\ rib\ i}$, where i corresponds to the barrier number (1, 2, 3, or 4). Additionally, all external ribs situated near the air gap are assumed to share uniform thicknesses, labeled $h_{out\ rib}$. This configuration ensures both magnetic performance and mechanical stability within the rotor design.

The rotor surface is demarcated with key reference points that play a pivotal role in defining the barrier geometry. Let us consider one flux barrier with its reference points. Points 1 and 1' are located at an angular distance α_i from the symmetry axis of the barrier.

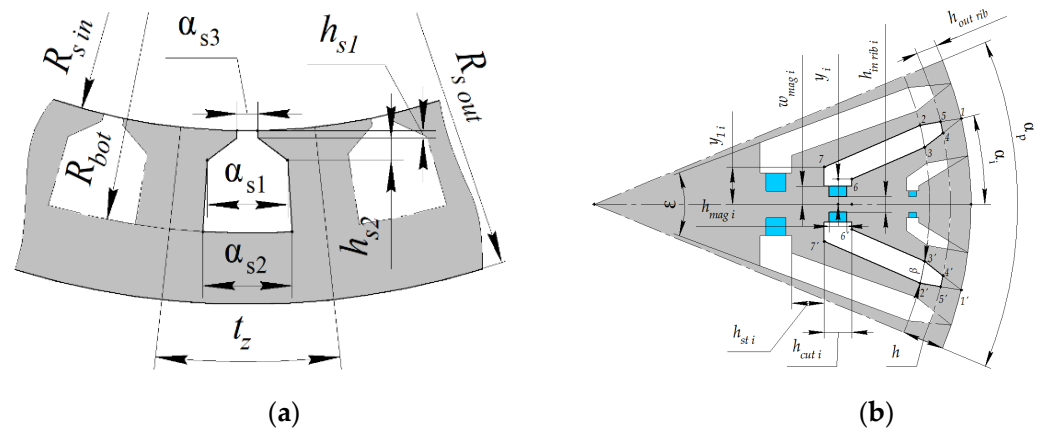


Figure 5. REaSynRM parameters: (a) stator; (b) rotor.

The points situated farther from the rotor surface at a distance h , specifically labeled as 2, 3, 2', and 3', are separated by an angular distance β from one another.

A circular demarcation referred to as 455'4' sets the barrier ends at the distance of the outer ribs' thickness $h_{out\ rib}$ from the outer rotor cylinder.

Lines 66' and 77' are perpendicular to the axes of symmetry. Unlike the internal rotor barriers, the outermost barrier has point 3 coinciding with point 6 and point 3' coinciding with point 6'. The term $h_{st\ i}$ ($i = 1, 2, 3$) denotes the steel thicknesses from the given barrier to another one. The distances between lines 66' and 77' are denoted as $h_{cut\ i}$, and the distances between points 6, 6', and 7, 7' are $2y_i$ and $2y_{1i}$, respectively ($i = 1, 2, 3, 4$). Thus, the geometry of the rotor is determined by a lot of parameters.

To simplify the optimization process and reduce the calculation time, the number of variables to be adjusted is reduced by introducing new parameters. These newly introduced parameters are linked to the previously mentioned parameters of individual magnetic barriers by means of new specific dependencies, thereby simplifying the overall optimization procedure while maintaining accuracy:

$$\begin{aligned}
 \alpha_i &= a + b(4 - i), i = 1, 2, 3, 4; \\
 y_{1i} &= y_i \cdot c, i = 1, 2, 3; \\
 y_i + 1 &= y_{1i} \cdot g, i = 1, 2, 3, 4; \\
 h_{cut\ i} &= a_{cut} + b_{cut} (i - 1), i = 1, 2, 3, 4; \\
 h_{st\ i} &= a_{st} + b_{st} (i - 1), i = 1, 2, 3.
 \end{aligned}
 \tag{4}$$

These new rotor parameters $a, b, c, g, a_{cut}, b_{cut}, a_{st}$, and b_{st} , defined by Equation (4), do not have geometric meaning. They are varied during optimization instead of the geometric parameters of individual barriers, which makes it possible to reduce the total number of optimization parameters. For the innermost (fourth) barrier, the angular distance ϵ between 7 and 7' is fixed during the optimization. Therefore, y_{14} is not determined by (5).

Additionally, the magnet thickness ratio ($h_{mag\ i}/h_{cut\ i}$) and the magnet width ratio ($w_{mag\ i}/y_i$) were assumed to be identical for all barriers. The parameter a in (5) is fixed during optimization to prevent the angular position of the fourth flux barrier α_4 from increasing too much and avoiding unfeasible geometries.

Figure 5a illustrates the geometric parameters of the stator. The stator slot width ratio is α_{s1}/α_{s2} assumed to be fixed.

During optimization, variable parameters also encompass current control angles at operating points 1, 2, 3, and 4. Fixed parameters of the REaSynRM are detailed in Table 4, while Table 5 outlines parameters subject to optimization.

Table 4. Parameters of the motor that remain constant during the optimization process.

Parameter	Value
Stator parameters	
Machine length excluding winding end parts L , mm	200
Stator outer radius $R_{s\ out}$, mm	250
Stator parameter h_{s1} , mm	1
Stator parameter h_{s2} , mm	3
Stator slot thickness ratio α_{s1}/α_{s2}	1.05
Rotor parameters	
Outer rotor ribs thickness $h_{out\ rib}$, mm	1
Inner rotor ribs thickness $h_{in\ rib\ i}$, mm	1.5; 2.5; 3.5; 4
Rotor parameter h , mm	3
Rotor parameter ε	$0.8 \cdot \alpha_p$
Rotor parameter a	$0.4777 \cdot \alpha_p$
Remanent flux density of the PMs, T	1.2
Relative magnetic conductivity of permanent magnets	1.05

The geometric meaning of the parameters is shown in Figure 5; α_p is the rotor pole pitch.

Table 5. Variable motor parameters.

Parameter	Initial Design	Optimized Design
Stator parameters		
Inner stator radius $R_{s\ in}$, m	0.2	0.1834
Stator slot bottom radius R_{bot} , m	0.23	0.2199
Stator slot thickness α_{s1}	$0.4 \cdot t_z$	$0.572 \cdot t_z$
Rotor parameters		
a_{st} , mm	4	4.46
b_{st} , mm	1	1.22
a_{cut} , mm	4	7.90
b_{cut} , mm	1	1.74
B	$0.0777 \cdot \alpha_p$	$0.0762 \cdot \alpha_p$
C	1.07	1.125
G	1.07	1.113
β , rad	0.01	0.0201
Magnet's thickness ratio, $h_{mag,i}/h_{cut,i}$	0.5	0.257
Magnet's width ratio, $w_{mag,i}/y_i$	0.5	0.485
Other parameters		
Air gap width δ , mm	1	2.33
Current angle, electrical degrees	50; 50; 50; 50	64.3; 66.8; 59.7; 55.6

Note: The geometric meaning of the parameters is shown in Figure 5; t_z is the stator slot pitch.

5.2. REaSynRM Optimization Results

Table 6 presents a comparative overview of the initial and refined designs of the REaSynRM, showing their distinctive characteristics.

During the open-circuit coasting phase, the voltage at the motor terminals registers a transformation from 273 V in the initial configuration to 274 V in the postoptimization one, which is much less than $V_{DC\ rated}$ in both cases. Notably, the concentration of magnetic loss density in this phase predominantly resides within the stator magnetic core, with a reduction from 1.67 kW to 0.8 kW during the optimization.

Table 6. REaSynRM performances before and after optimization.

Parameter	Before Optimization				
	1	2	3	4	5
Operating point, i	1	2	3	4	5
Rotational speed n , rpm	4280	4280	2854	0	1427
Amplitude of the armature phase current I_{arm} , A	483	876	1377	1388	1395
Efficiency, %	92.3	93.3	93.7	0	92.4
Output mechanical power P_2 , kW	185.3	−370.6	−370.6	0	185.3
Torque, N·m	413	827	1240	0	1240
Input electrical power, kW	200.7	345.7	347.3	11.3	200.5
Mechanical loss, kW *	3.55	3.55	1.06	0	0.14
Armature copper loss, kW	1.29	4.67	11.31	11.31	11.31
Stator lamination loss, kW	9.68	15.09	9.95	0	3.46
Rotor lamination loss, kW	0.91	1.61	1.02	0	0.26
Total loss, kW	15.42	24.92	23.35	11.31	15.16
Rotational speed n , rpm	4280	4280	2854	0	1427
Average losses $\langle P_{loss} \rangle$, kW			11.11		
Number of turns in armature winding			1.75		
Power factor	0.83	0.75	0.65	0	0.64
Line-to-line voltage amplitude V_{arm} , V	621.3	757.5	600.1	9.4	307.6
Torque ripple, %	31.6	32.6	33.2	33.2	33.2
Parameter	After Optimization				
Rotational speed n , rpm	4280	4280	2854	0	1427
Amplitude of the armature phase current I_{arm} , A	445	709	896	888	894
Efficiency, %	94.9	95.5	95.9	0	95.0
Output mechanical power P_2 , kW	185.3	−370.6	−370.6	0	185.3
Torque, N·m	413	827	1240	0	1240
Input electrical power, kW	195.2	353.9	355.5	7.0	195.0
Mechanical loss, kW *	3.55	3.55	1.06	0	0.14
Armature copper loss, kW	1.69	4.56	7.21	6.97	6.97
Stator lamination loss, kW	4.11	7.75	6.57	0	2.59
Rotor lamination loss, kW	0.55	0.86	0.27	0	0.06
Total loss, kW	9.90	16.72	15.11	6.97	9.75
Average losses $\langle P_{loss} \rangle$, kW			7.63		
Number of turns in armature winding			2.77		
Power factor	0.86	0.79	0.71	0	0.69
Line-to-line voltage amplitude V_{arm} , V	626.1	757.5	708.5	9.1	365.9
Torque ripple, %	17.8	17.8	14.3	15.3	15.3

Note: * It is assumed that mechanical loss increases proportionally to the cube of the speed, reaching a maximum value of 3.55 kW at n_{max} .

In addition to that, Figure 6 showcases the REaSynRM geometry and flux density amplitude in operational points 0–5 detailed in Table 1. Meanwhile, Figure 7 presents a visual comparison of the geometry and flux density amplitude after the REaSynRM optimization.

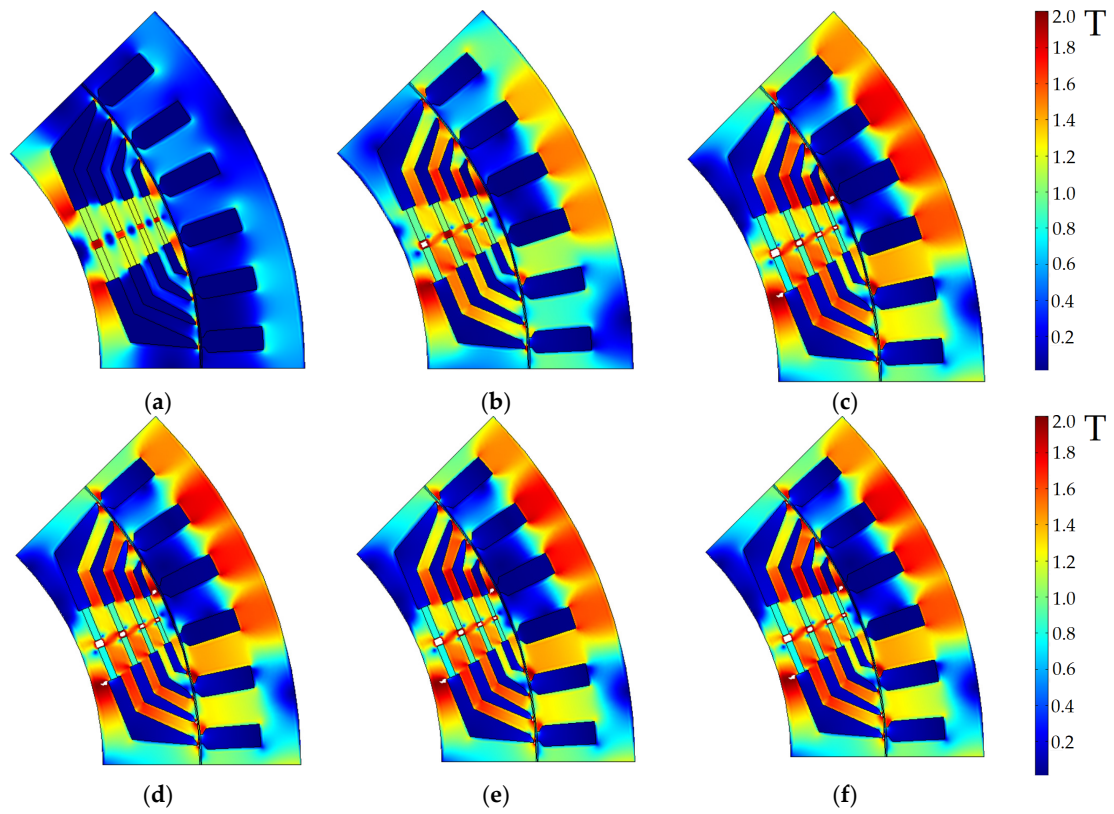


Figure 6. Cross-section of the REaSynRM before optimization, with the flux density magnitude at the saturation limit (greater than 2 T) highlighted in white: (a) operating point 0; (b) operating point 1; (c) operating point 2; (d) operating point 3; (e) operating point 4; (f) operating point 5.

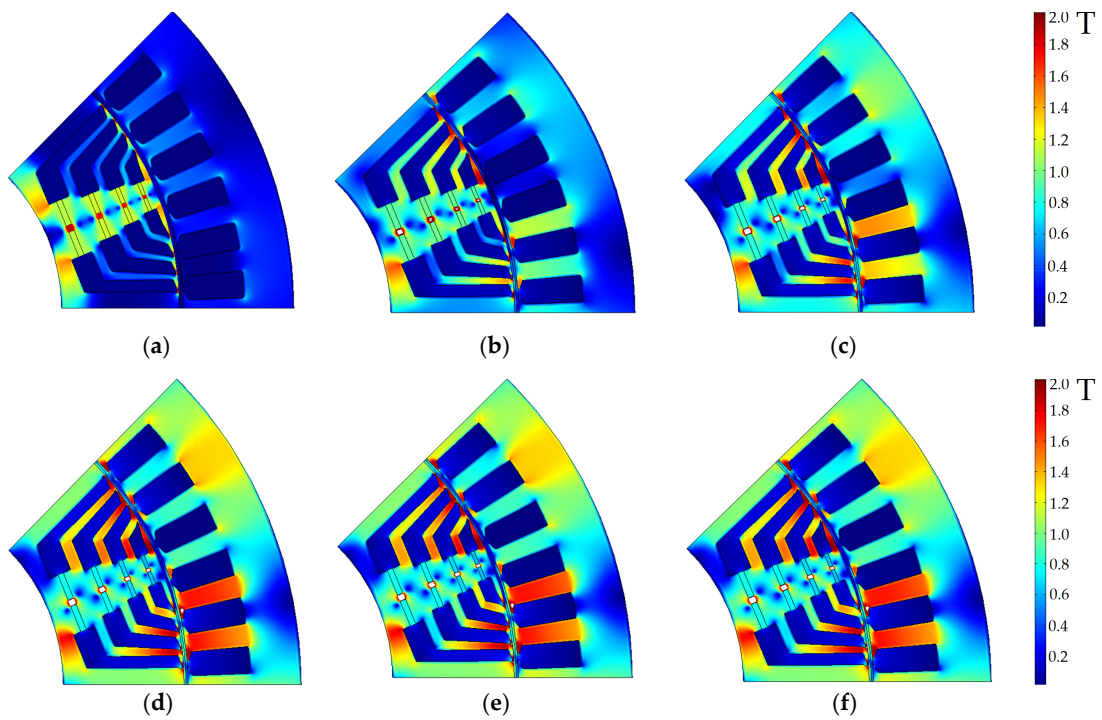


Figure 7. Cross-section of the REaSynRM after optimization, with the flux density magnitude at the saturation limit (greater than 2 T) highlighted in white: (a) operating point 0; (b) operating point 1; (c) operating point 2; (d) operating point 3; (e) operating point 4; (f) operating point 5.

Furthermore, Figure 8 delves into the picture of the demagnetizing field encompassing the region of permanent magnets on the rotor, which does not exceed 8.1 kOe. Figure 9 shows the REaSynRM torque ripple and cogging torque waveforms calculated by FEA.

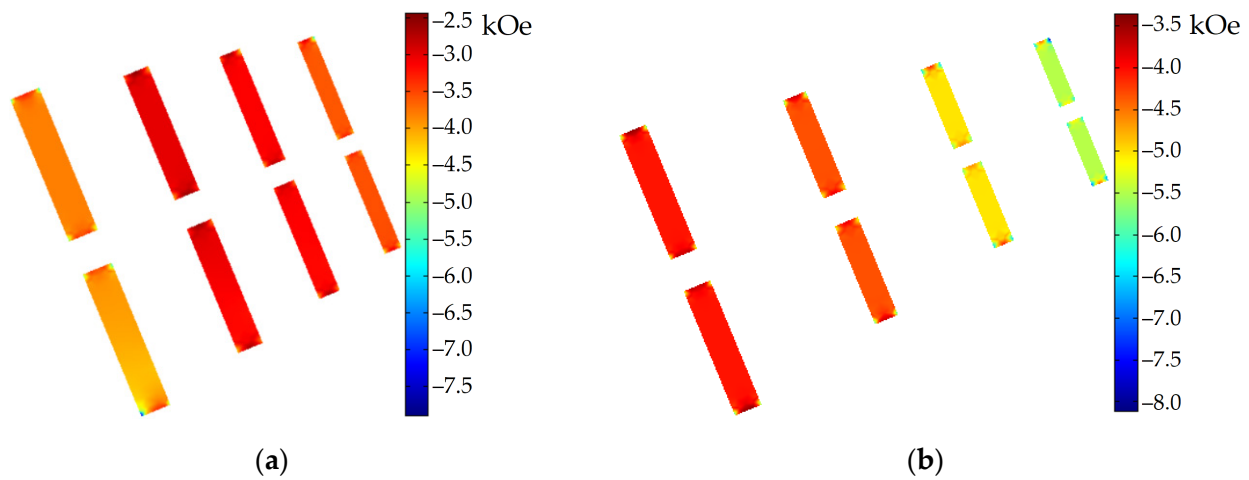


Figure 8. Demagnetizing field in the area of permanent magnets of the REaSynRM rotor: (a) before optimization; (b) after optimization in operation point 4.

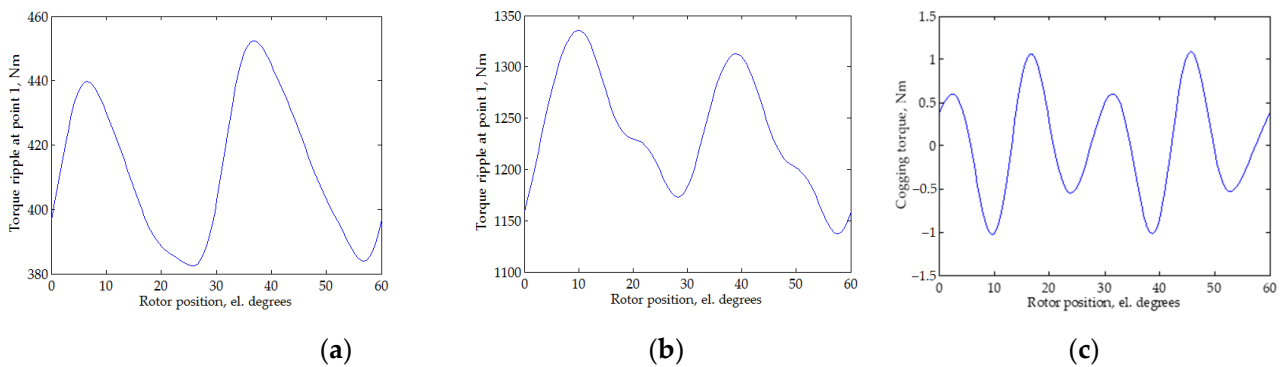


Figure 9. REaSynRM waveforms calculated using FEA: (a) torque ripple at operating point 1; (b) torque ripple at operating point 4; (c) cogging torque at coasting.

The significant advantage of PMSynRM, in comparison with IPM, is that the emergency short circuit mode of a PMSynRM does not pose danger in terms of unacceptable current levels, overheating, or fire of the winding. In this case, there is also no risk of irreversible demagnetization. To confirm this, the asymptotic short circuit mode at infinite speed is calculated. In this case, the magnetic fluxes through the phase windings are zero, and the current value is determined by Lenz's rule.

Figure 10 shows 2D plots of flux density and demagnetizing force in the permanent magnet region for the short circuit. Figure 11 shows the voltage and current waveforms for this case. The RMS value of the short-circuit current is 250 A, and its amplitude is 350 A, which is much less than the operating current amplitude, which is in the range of 445–896 A depending on the load point (see Table 6). The short circuit winding loss is 1.09 kW. The demagnetizing field does not exceed 3.3 kOe. These values are significantly less than underload. The magnetic flux of magnets in short-circuit mode is closed through sections of magnetic barriers unoccupied by magnets. In addition, the winding does not completely block the flux through the stator yoke due to slot leakage.

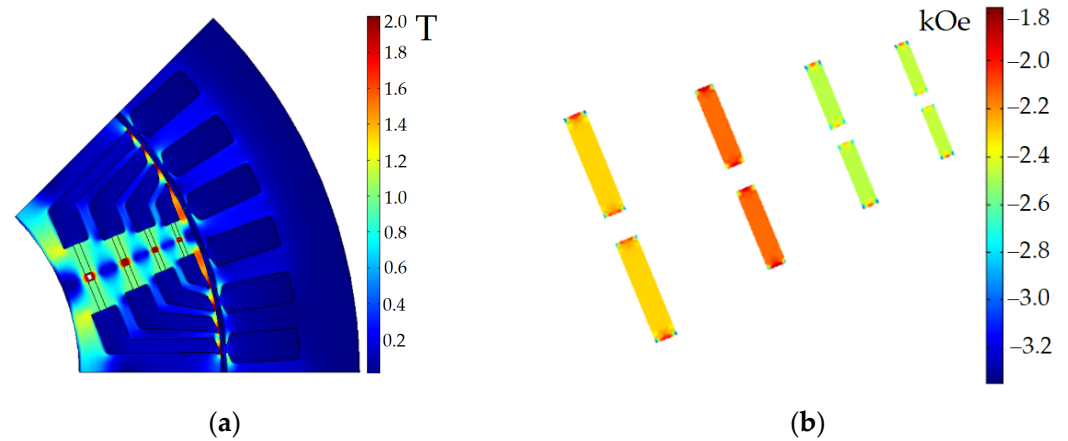


Figure 10. REaSynRM plots at short circuit: (a) flux density modulus (T); (b) demagnetization field (kOe).

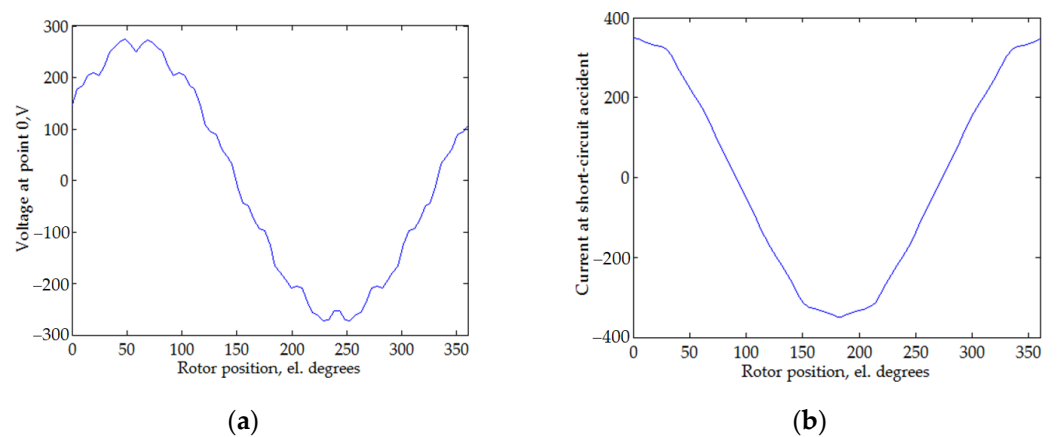


Figure 11. REaSynRM waveforms in short circuit mode: (a) phase voltage; (b) phase current.

By comparing the performance of the REaSynRM before and after optimization, several key observations can be made about how changes implemented during the optimization process affected its performance:

- (1) The average losses after optimization were reduced by $100\% \times (11.11 - 7.63)/11.11 = 31.3\%$;
- (2) The core loss during the train coasting decreases by $1.67/0.8 = 2.1$ times;
- (3) The maximum current consumption by the motor from the traction inverter decreased by $100\% \times (1395 - 896)/1395 = 35.7\%$;
- (4) The maximum torque ripple decreased by $33.2 - 15.3 = 17.9\%$;
- (5) In the emergency short-circuit mode, the loss in the winding is $(1.29 - 1.09)/1.29 = 15.5\%$ less than in operating point 1 (high-speed motor mode), in which the loss is significantly less than in the full torque operating point, and the demagnetizing force is $8.1/3.3 = 2.5$ times less.

6. Performance Comparison of the REaSynRM and FaSynRM

This section compares the REaSynRM characteristics obtained in this study with the FaSynRM characteristics obtained in our previous study [16]. Tables 7 and 8 compare the performance characteristics of FaSynRM and REaSynRM in the subway driving cycle. The optimized characteristics of FaSynRM are adopted from [16]. The optimized characteristics of the REaSynRM are taken from Table 6. The comparative analysis presented in Table 9 briefly illustrates the differences in weight, size, and cost of the active materials.

Table 7. Characteristics of the optimized FaSynRM.

Parameter	Operating Point, <i>i</i>					
	0	1	2	3	4	5
Rotational speed <i>n</i> , rpm	4280	4280	4280	2854	0	1427
Amplitude of the armature phase current <i>I_{arm}</i> , A	0	450	693	833	832	839
Efficiency η , % *	-	94.7	95.4	96.0	0	95.3
Output mechanical power <i>P₂</i> , kW	-4.19	185.3	-370.6	-370.6	0	185.3
Torque <i>T</i> , N·m	0	413.4	826.9	1240	1240	1240
Input electrical power <i>P₁</i> , kW	0	195.6	353.5	355.9	6.2	194.4
Mechanical loss <i>P_{mech}</i> , kW	3.55	3.55	3.55	1.06	0	0.14
Armature copper loss <i>P_{arm DC}</i> , kW	0	1.76	4.44	6.37	6.22	6.22
Stator lamination loss <i>P_{iron st}</i> , kW	0.49	4.25	7.88	6.89	0	2.70
Rotor lamination loss <i>P_{iron rt}</i> , kW	0	0.77	1.21	0.33	0	0.07
Total loss <i>P_{loss}</i> , kW **	4.04	10.33	17.08	14.65	6.22	9.12
Average losses $\langle P_{loss} \rangle$, kW			7.40			
Power factor	-	0.910	0.791	1	0.769	0.735
Line-to-line voltage amplitude <i>V_{arm}</i> , V	-	621	757	665	9	356
Torque ripple, %	-	16	16	11	10	10
Maximum demagnetizing force, kOe			2.0			

Note: * the PMSynRM efficiency is calculated as $\eta = P_2/P_1 = P_2/(P_2 + P_{loss})$, where *P₁* is the active power in armature winding; *P₂* is the output (mechanical) power. ** The total loss for PMSynRM is calculated as a sum of the following $P_{loss} = P_{arm DC} + P_{iron st} + P_{iron rt} + P_{mech}$.

Table 8. Characteristics of the optimized REaSynRM.

Parameter	Operating Point, <i>i</i>					
	0	1	2	3	4	5
Rotational speed <i>n</i> , rpm	4280	4280	4280	2854	0	1427
Amplitude of the armature phase current <i>I_{arm}</i> , A	0	445	709	896	888	894
Efficiency η , % *	-	94.9	95.5	95.9	0	95.0
Output mechanical power <i>P₂</i> , kW	-4.35	185.3	-370.6	-370.6	0	185.3
Torque <i>T</i> , N·m	0	413	827	1240	0	1240
Input electrical power <i>P₁</i> , kW	0	195.2	353.9	355.5	7.0	195.0
Mechanical loss <i>P_{mech}</i> , kW	3.55	3.55	3.55	1.06	0	0.14
Armature copper loss <i>P_{arm DC}</i> , kW	0	1.69	4.56	7.21	6.97	6.97
Stator lamination loss <i>P_{iron st}</i> , kW	0.79	4.11	7.75	6.57	0	2.59
Rotor lamination loss <i>P_{iron rt}</i> , kW	0.1	0.55	0.86	0.27	0	0.06
Total loss <i>P_{loss}</i> , kW **	4.35	9.90	16.72	15.11	6.97	9.75
Average losses $\langle P_{loss} \rangle$, kW			7.63			
Power factor	-	0.86	0.79	0.71	0	0.69
Line-to-line voltage amplitude <i>V_{arm}</i> , V	-	626.1	757.5	708.5	9.1	365.9
Torque ripple, %	-	17.8	17.8	14.3	15.3	15.3
Maximum demagnetizing force, kOe			8.1			

Note: * the PMSynRM efficiency is calculated as $\eta = P_2/P_1 = P_2/(P_2 + P_{loss})$, where *P₁* is the active power in armature winding; *P₂* is the output (mechanical) power. ** The total loss for PMSynRM is calculated as a sum of the following $P_{loss} = P_{arm DC} + P_{iron st} + P_{iron rt} + P_{mech}$.

Table 9. Operating cycle points for the subway train drive considered in the optimization.

Parameter	FaSynRM	REaSynRM
Stator lamination mass, kg	104.6	100.8
Rotor lamination mass, kg	78.4	61.3
Armature copper mass, kg	38	41.7
Magnets mass, kg	20	3.11
Total rotor material mass, kg	98.4	64.4
The total mass of the active materials, kg	241	206.9
Stator lamination cost, USD	104.6	100.8

Table 9. Cont.

Parameter	FaSynRM	REaSynRM
Rotor lamination cost, USD	78.4	61.3
Armature copper cost, USD	266	291.9
Magnets cost, USD	369.2	393.7
The total cost of the active materials, USD *	818.2	847.72
Total length of the stator lamination L , mm	240	200
Stator lamination outer diameter D , mm	500	500
Air gap, mm	2.23	2.33

Note: * In conducting a material cost analysis of the traction motor variants, this study considered three types of materials: copper used in the motor windings (7 USD/kg); electrical steel used as the main material of the magnetic core (1 USD/kg); and two types of magnets (rare earth N40H, 126.6 USD/kg, and ferrite Y30H-2, 18.46 USD/kg). The specific prices associated with these materials are based on references [16,30,31], which provide an indication of the current market value of such materials.

Comparing the characteristics of the FaSynRM and REaSynRM with the same outer diameter presented in Tables 7–9, we can draw the following conclusions:

- (1) The selected length of the REaSynRM, excluding the winding end parts, is shorter than that of the FaSynRM by $(24 - 20)/24 = 17\%$, while the torque density and efficiency are close to those of the FaSynRM [16];
- (2) In this application, the average loss of the REaSynRM is $100\% \times (7.63 - 7.40)/7.63 = 3.0\%$ greater than that of the FaSynRM;
- (3) The maximum armature current for the REaSynRM is $100\% \times (896 - 839)/896 = 6.4\%$ greater than for the FaSynRM;
- (4) The mass of the REaSynRM rotor is $100\% \times (98.4 - 64.4)/98.4 = 34.5\%$ less than that of the FaSynRM. This will ensure a longer service life of the bearings in the case of the REaSynRM;
- (5) Due to the full use of the higher potential of rare earth magnets, the mass of the magnets in the REaSynRM is reduced by 6.4 times compared to the FaSynRM. As a result, the cost of rare-earth magnets is only $(393.7 - 369.2)/393.7 = 6.2\%$ higher than the cost of ferrites in the FaSynRM, while a ratio of their prices per kg of $126.6/18.46 = 6.9$ times;
- (6) The total mass of the REaSynRM active materials is $100\% \times (241 - 206.9)/241 = 14.1\%$ less than that of the FaSynRM;
- (7) In comparison to the FaSynRM, the REaSynRM incurs a $100\% \times (847.7 - 818.2)/847.7 = 3.5\%$ increase in total material costs. This suggests that there is no significant increase in the cost of the REaSynRM, which is achieved by reducing the mass of the magnets compared to the FaSynRM with the reasonable use of this small amount of rare-earth magnets.

7. Conclusions

This paper discusses the optimal design of the permanent magnet-assisted synchronous reluctance motor (PMSynRM) with rare earth magnets (REaSynRM) for subway train drive. Its performance is also compared with a SynRM with ferrite magnets (FaSynRM). Both motors have the same outer diameter.

The optimization of these machines is carried out considering the dynamic cycle of the train's movement. To make this process more computationally efficient, the Nelder–Mead method is employed. During each iteration of the optimization, the machine's characteristics are calculated at just six specific operating points. By using quadrature formulas, this approach allows for the comprehensive derivation of integral machine characteristics over the entire motion cycle, despite the limited number of points considered.

When parameterizing the REaSynRM rotor geometry for optimization, it must be considered that:

- High coercivity helps reduce magnet thickness without the risk of irreversible demagnetization.
- Due to their high remanent flux density, rare earth magnets produce sufficient magnetic flux even when placed into a short section of magnetic barriers.

Therefore, to optimize the REaSynRM, a geometry parameterization has been developed in which the dimensions of the magnets are selected independently of most of the dimensions of nonmagnetic barriers, specifying small narrowings of the barriers for placement of magnets.

The optimization goals involve a detailed approach aimed at reducing losses across the entire motion cycle of the train, minimizing peak current in the semiconductor inverter, and mitigating torque ripple effects. This thorough analysis seeks to offer a comprehensive comparison of the REaSynRM and FaSynRM designs, highlighting their respective advantages and disadvantages within the intricate field of subway train traction drives.

As a result of optimization, it is demonstrated that the possibility of developing the REaSynRM with comparable characteristics of the FaSynRM (losses are 3% more, maximum current is 6.4% more) with significantly improved weight and dimensions: the length of the motor excluding the winding end parts is reduced by $(24 - 20)/24 = 17\%$, and the total mass of active materials is reduced by 14.1%.

Due to the full use of the potential of rare-earth magnets, the magnet mass is reduced by 6.4 times in the REaSynRM compared to the FaSynRM. As a result, the price of rare-earth magnets in the REaSynRM is only 6.2% higher than the price of ferrite magnets in the FaSynRM, with the ratio of their specific prices being 6.9 times. The total costs of the active materials of both machines are almost equal (by 100% $(847.7 - 818.2)/847.7 = 3.5\%$ higher for the REaSynRM). The REaSynRM also has a 34.5% lower rotor weight, which will ensure longer service life of the bearings.

Author Contributions: Conceptual approach, A.A., V.D. and V.P.; data curation, V.D. and V.K.; software, V.D. and V.P.; calculations and modeling, A.A., V.D., V.K. and V.P.; writing—original draft, A.A., V.D., V.K. and V.P.; visualization, V.D. and V.K.; review and editing, A.A., V.D., V.K. and V.P. All authors have read and agreed to the published version of the manuscript.

Funding: The research funding from the Ministry of Science and Higher Education of the Russian Federation (Ural Federal University Program of Development within the Priority-2030 Program) is gratefully acknowledged.

Data Availability Statement: The original contributions presented in the study are included in the article, further inquiries can be directed to the corresponding author.

Acknowledgments: The authors thank the editors and reviewers for carefully reading and providing constructive comments.

Conflicts of Interest: The authors declare no conflicts of interest.

References

1. Railway Pro. Alstom Tests a New Train Traction System in China. Press Release. 29 May 2023. Available online: <https://www.railwaypro.com/wp/alstom-tests-a-new-train-traction-system-in-china/> (accessed on 5 September 2024).
2. Körner, O.; Schmidt, D.; Wetzels, W. Energy efficient propulsion technology based on permanent magnet synchronous motors. *Eng. Veh. Technol.* **2023**, *121*, 296–304. Available online: <https://assets.new.siemens.com/siemens/assets/api/uuid:d699a038-d754-46d1-9c17-7241daa549ca/siemens-mobility-Energy-efficient-propulsion-technology-eb-technical-article-en-original..pdf> (accessed on 5 September 2024).
3. Toshiba Global. Permanent Magnet Synchronous Motor (PMSM). Supply Record. Available online: <https://www.global.toshiba/ww/products-solutions/railway/rolling-stock/pmsm.html> (accessed on 5 September 2024).
4. Tokyo Metro Tested Synchronous Reluctance Traction Motors. Railvolution: The Professional On-Line Magazine of Rail Transport Worldwide. Available online: <https://www.railvolution.net/news/tokyo-metro-tested-synchronous-reluctance-traction-motors> (accessed on 5 September 2024).

5. Wang, Y.; Bianchi, N.; Qu, R. Comparative Study of Non-Rare-Earth and Rare-Earth PM Motors for EV Applications. *Energies* **2022**, *15*, 2711. [[CrossRef](#)]
6. Burress, T.; Campbell, S. Benchmarking EV and HEV power electronics and electric machines. In Proceedings of the 2013 IEEE Transportation Electrification Conference and Expo (ITEC), Detroit, MI, USA, 16–19 June 2013; pp. 1–6.
7. Calvo, E.S.; Potoradi, D. Synchronous reluctance motors with and without permanent magnets for high performance low cost electrical drives. In Proceedings of the 2015 5th International Electric Drives Production Conference (EDPC), Nuremberg, Germany, 15–16 September 2015.
8. Liu, Z.; Hu, Y.; Wu, J.; Zhang, B.; Feng, G. A Novel Modular Permanent Magnet-Assisted Synchronous Reluctance Motor. *IEEE Access* **2022**, *9*, 19947–19959. [[CrossRef](#)]
9. Barcaro, M.; Pradella, T.; Furlan, I. Low-torque ripple design of a ferrite-assisted synchronous reluctance motor. *IET Electr. Power Appl.* **2016**, *10*, 319–329. [[CrossRef](#)]
10. Pellegrino, G.; Jahns, T.M.; Bianchi, N.; Soong, W.L.; Cupertino, F. *The Rediscovery of Synchronous Reluctance and Ferrite Permanent Magnet Motors: Tutorial Course Notes*; Springer: New York, NY, USA, 2016; p. 136.
11. McKinsey & Company. The Net-Zero Materials Transition: Implications for Global Supply Chains, Report. July 2023. Available online: <https://www.mckinsey.com/industries/metals-and-mining/our-insights/the-net-zero-materials-transition-implications-for-global-supply-chains> (accessed on 14 August 2024).
12. Dong, S.; Li, W.; Chen, H.; Han, R. The status of Chinese permanent magnet industry and R&D activities. *AIP Adv.* **2017**, *7*, 1–17.
13. Ibrahim, M.N.; Silwal, B.; Sergeant, P. Permanent Magnet-Assisted Synchronous Reluctance Motor Employing a Hybrid Star-Delta Winding for High Speed Applications. In Proceedings of the 2018 XIII International Conference on Electrical Machines (ICEM), Alexandroupoli, Greece, 3–6 September 2018.
14. Li, Y.; Yang, H.; Lin, H.; Fang, S.; Wang, W. A Novel Magnet-Axis-Shifted Hybrid Permanent Magnet Machine for Electric Vehicle Applications. *Energies* **2019**, *12*, 641. [[CrossRef](#)]
15. Liu, X.; Li, Y.; Liu, Z.; Ling, T.; Luo, Z. Analysis and design of a high power density permanent magnet-assisted synchronous reluctance machine with low-cost ferrite magnets for EVs/HEVs. *COMPEL Int. J. Comput. Math. Electr. Electron. Eng.* **2016**, *35*, 1949–1964. [[CrossRef](#)]
16. Dmitrievskii, V.; Kazakbaev, V.; Prakht, V. Performance Comparison of Traction Synchronous Motors with Ferrite Magnets for a Subway Train: Reluctance versus Homopolar Variants. *Appl. Sci.* **2023**, *13*, 9988. [[CrossRef](#)]
17. Wang, J.; Yuan, X.; Atallah, K. Design Optimization of a Surface-Mounted Permanent-Magnet Motor with Concentrated Windings for Electric Vehicle Applications. *IEEE Trans. Veh. Technol.* **2013**, *62*, 1053–1064. [[CrossRef](#)]
18. Lacock, S.; du Plessis, A.A.; Booyesen, M.J. Electric Vehicle Drivetrain Efficiency and the Multi-Speed Transmission Question. *World Electr. Veh. J.* **2023**, *14*, 342. [[CrossRef](#)]
19. Guo, S.; Zhao, H.; Wang, Y.; Yin, X.; Qi, H.; Li, P.; Lin, Z. A Design Technique of Traction Motor for Efficiency Improvement Based on Multiobjective Optimization. *World Electr. Veh. J.* **2021**, *12*, 260. [[CrossRef](#)]
20. Ramakrishnan, K.; Stipetic, S.; Gobbi, M.; Mastinu, G. Optimal Sizing of Traction Motors Using Scalable Electric Machine Model. *IEEE Trans. Transp. Electr.* **2018**, *4*, 314–321. [[CrossRef](#)]
21. Dmitrievskii, V.; Prakht, V.; Kazakbaev, V.; Anuchin, A. Design Optimization of the Magnet-Free Synchronous Homopolar Motor of a Subway Train. *Appl. Sci.* **2022**, *12*, 12647. [[CrossRef](#)]
22. Dmitrievskii, V.; Prakht, V.; Kazakbaev, V. Design Optimization of a Synchronous Homopolar Motor with Ferrite Magnets for Subway Train. *Mathematics* **2023**, *11*, 589. [[CrossRef](#)]
23. Moghaddam, R.R. Synchronous Reluctance Machine (SynRM) Design. Thesis for the Degree of Master of Science in Engineering, Royal Institute of Technology, Department of Electrical Engineering, Electrical Machines and Power Electronics, Stockholm. 2007. Available online: <https://www.diva-portal.org/smash/get/diva2:753114/FULLTEXT01.pdf> (accessed on 14 August 2024).
24. Wogi, L.; Thelkar, A.; Tahiro, T.; Ayana, T.; Urooj, S.; Laguech, S. Particle Swarm Optimization Based Optimal Design of Six-Phase Induction Motor for Electric Propulsion of Submarines. *Energies* **2022**, *15*, 2994. [[CrossRef](#)]
25. Kang, Y.-R.; Son, J.-C.; Lim, D.-K. Optimal Design of IPMSM for Fuel Cell Electric Vehicles Using Autotuning Elliptical Niching Genetic Algorithm. *IEEE Access* **2020**, *8*, 117405–117412. [[CrossRef](#)]
26. Prakht, V.; Dmitrievskii, V.; Kazakbaev, V.; Anuchin, A. Comparative Study of Electrically Excited Conventional and Homopolar Synchronous Motors for the Traction Drive of a Mining Dump Truck Operating in a Wide Speed Range in Field-Weakening Region. *Mathematics* **2022**, *10*, 3364. [[CrossRef](#)]
27. Lagarias, J.C.; Reeds, J.A.; Wright, M.H.; Wright, P.E. Convergence properties of the Nelder–Mead simplex method in low dimensions. *SIAM J. Optim.* **1998**, *9*, 112–147. [[CrossRef](#)]
28. The MathWorks, Inc. Find Minimum of Unconstrained Multivariable Function Using Derivative-Free Method. MATLAB Documentation. 1994–2023. Available online: <https://www.mathworks.com/help/matlab/ref/fminsearch.html> (accessed on 14 August 2024).
29. Prakht, V.; Dmitrievskii, V.; Kazakbaev, V. Mathematical modeling ultra premium efficiency (IE5 class) PM assisted synchronous reluctance motor with ferrite magnets. In Proceedings of the 2018 25th International Workshop on Electric Drives: Optimization in Control of Electric Drives (IWED), Moscow, Russia, 31 January–2 February 2018; pp. 1–6. [[CrossRef](#)]

30. ChenYang NdFeB Magnets. Price List of Standard Block Magnets. Available online: <http://www.ndfebagnets.de/CY-PriceList-NdFeB-Block.pdf> (accessed on 14 August 2024).
31. IBSMagnet. Hard Ferrite Magnets, Product Information. 2020. Available online: <https://ibsmagnet.com/products/dauermagnete/hartferrit.php> (accessed on 14 August 2024).

Disclaimer/Publisher's Note: The statements, opinions and data contained in all publications are solely those of the individual author(s) and contributor(s) and not of MDPI and/or the editor(s). MDPI and/or the editor(s) disclaim responsibility for any injury to people or property resulting from any ideas, methods, instructions or products referred to in the content.